J. Meas. Sci. Instrum., 2025, 16(4): 588-602. http://jmsi.publish.founderss.cn
DOI: 10.62756/jmsi.1674-8042.2025057 jmsi@nuc.edu.cn

Simulation-based parameter optimization and development of a split-core fluxgate DC current sensor

YANG Dechao[1], SHI Junjiang[1], ZHAO Zhengang[1,2*], HOU Yingjie[1], YANG Kuisong[1], JIANG Xin[1]

1. Faculty of Information Engineering and Automation, Kunming University of Science and Technology, Kunming 650500, China;
2. Yunnan Key Laboratory of Green Energy, Electric Power Measurement Digitalization, Control and Protection, Kunming 650500, China

***Corresponding author:** ZHAO Zhengang (zhaozhengang@kust.edu.cn)

Received: February 9, 2025 **Revised:** April 3, 2025 **Accepted:** May 12, 2025

Abstract: Fluxgate current sensors (FGCSs) are increasingly employed in power systems due to their high-precision characteristics, yet their measurement flexibility remains constrained by conventional closed-core designs. To address this limitation, we proposed a split-core sensor structure comprising four magnetic core strips, which achieved non-intrusive current measurement while maintaining detection accuracy. An analytical model of the induced electromotive force was established based on the probe's geometric configuration, followed by finite element simulations to optimize key parameters including core radius, core width, excitation coil turns, and sensing coil configuration. A complete prototype integrating the measurement probe, excitation circuit, and signal processing circuitry was developed and experimentally validated. The experimental results show a sensitivity of 0.109 9 V/A, a hysteresis error of 0.559%, and a repeatability error of 1.574% over a measurement range of ±10 A. After polynomial fitting-based error compensation, the nonlinearity error was reduced to 0.208%, achieving performance comparable to closed-core sensors. This work provided a practical solution for applications demanding both high measurement accuracy and installation flexibility.

Key words: fluxgate current sensor; second harmonic method; finite element simulation; parameter optimization; circuit design; DC measurement

0 Introduction

Accurate current measurement has become increasingly critical with the widespread adoption of various direct current (DC) devices. Consequently, multiple instruments have been developed to measure DC currents accurately[1-4]. Among current sensors based on different operating principles, those that indirectly measure current by detecting changes in the external magnetic field are now widely used, including Hall current sensors (HCSs), fluxgate current sensors (FGCSs), current transformers (CTs), and Rogowski coil current transducers (RCCTs)[5-8]. Of these sensors, HCSs and FGCSs are suitable for DC measurement. Unlike HCSs, FGCSs operate on the principle of electromagnetic induction, requiring an alternating excitation signal to periodically saturate their internal magnetic core. The external magnetic field changes are then measured indirectly to determine the magnitude and direction of the current[9]. A typical FGCS comprises a measurement probe, an excitation circuit, and a signal processing circuit. Owing to the high sensitivity of permeable materials to magnetic fields, FGCSs achieve enhanced detection capabilities and have been increasingly applied in magnetic field and current measurements[10-12].

Common configurations of FGCSs primarily include self-oscillating, excitation-induction, and magnetic flux concentrator types[13-15]. The magnetic core structure of the above fluxgate current sensors is usually designed to have a closed magnetic loop[16]. This design ensures that magnetic flux lines are evenly distributed within the core, minimizes interference from external magnetic fields, reduces hysteresis effects, and enhances sensitivity. However, sensors with this configuration are typically installed in fixed positions to monitor the current of specific lines, such as the output current of electrical energy devices, electrical energy measurement in medical devices or the residual current of battery packs in electric vehicles, thereby limiting their application scope.

To address these limitations, significant research

efforts have been made. Lei et al. developed a dual-magnetic-circuit current sensor with combined openable-closable configurations, incorporating dual excitation-detection coil sets to enhance external magnetic field sensitivity[17]. This design enables precise measurement of weak currents ranging from microamperes (μA) to milliamperes (mA). Although Song et al. proposed an open-magnetic-circuit current sensor, its unoptimized structure resulted in limited measurement range[18].

A structure with two symmetrical open magnetic circuits with a dual-core was designed. This design guaranteed that the induction coil collected higher second harmonic components while leaving space for the addition of feedback coils. The feasibility was verified through finite element analysis (FEA), which evaluated key parameters of the non-closed core structure, including the core size, the number of turns in the excitation coil, the winding method of the induction coil, and the number of turns in the induction coil. Ultimately, the current sensor probe, excitation circuit, and signal processing circuit are constructed based on the design parameters, completing the overall sensor assembly and achieving the linearity of less than 1% under operating conditions, while also achieving satisfactory sensitivity and repeatability, to validate the practical significance of the research.

1 Measuring principle and mathematical model construction

The main components of an FGCS are the probe and the circuit. The probe core is made of high-permeability material, with the excitation, induction, and feedback coil uniformly wound on a resin skeleton that encases and supports the magnetic core.

A current-carrying wire generates a magnetic field in its surrounding space, with the magnitude depending on the current flowing through the wire and the distance from the wire[19]. When the sensor is activated, positive and negative square wave signals are applied to the excitation coil at a frequency of f_{ex}, generating an alternating magnetic field that causes the core to reach an alternating saturation state. The change in the external magnetic field is detected by extracting the second harmonic component of the induced electromotive force (IEMF). By processing the IEMF, the external circuit generates a voltage signal that accurately reflects both the magnitude and direction of the measured current. The overall split-core structure of the sensor is shown in Fig.1.

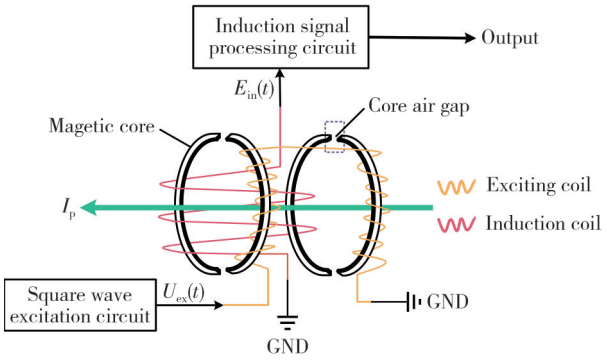

Fig. 1 Split-core structure diagram of sensor

The core section consists of four strips of permalloy tape, each bent into a semicircular ring. Assuming each core has an radius of r, and there are four air gaps. A magnetic field is generated at the air gaps, along the core, and in the surrounding space when the wire under test carries a current of I_p. This relationship is derived from Ampère's loop law.

$$I_p = 4H_{cp}l_c + 4H_{sp}l_s, \tag{1}$$

where H_{cp} represents the magnetic field generated by the current to be measured at the core, l_c is the average magnetic circuit length of each core and H_{sp} denotes the magnetic field generated by the current at the air gap of the core, with l_s being the air gap width. l_c can be expressed as

$$l_c = -l_s + \pi r. \tag{2}$$

The magnetic field H_{cp} generated by the current at the core can be determined by Eq. (1).

$$H_{cp} = \frac{I_p - 4H_{sp}l_s}{4\pi r - 4l_s}. \tag{3}$$

Assuming the excitation is driven by a bipolar square wave signal with amplitude U_{ex} and excitation frequency (EF) f_{ex}, the corresponding Fourier series is expressed as

$$f_{ex}(t) = \frac{4}{\pi}U_{ex}\sum_{n=1,3,5,\ldots}^{\infty}\frac{1}{n}\sin(2\pi n f_{ex}t). \tag{4}$$

If the fundamental wave component $4U_{ex}/\pi \cdot \sin(2\pi f_{ex}t)$ is used as the excitation signal, then according to Ampère's circuital law, in the case of ignoring the inductance effect of the coil, the excitation coil with internal resistance R_1 will generate excitation magnetic field strengths H_1 and H_2, which can be expressed as

$$\begin{aligned} H_1 &= \frac{\frac{4U_{ex}}{\pi R_1}\sin(2\pi f_{ex}t) - 4H_{se}l_s}{4\pi r - 4l_s}, \\ H_2 &= \frac{-\frac{4U_{ex}}{\pi R_1}\sin(2\pi f_{ex}t) - 4H_{se}l_s}{4\pi r - 4l_s}, \end{aligned} \tag{5}$$

where H_{se} represents the magnetic field generated by the excitation coil at the core air gap.

The magnetic field distribution on the core is shown in Fig.2.

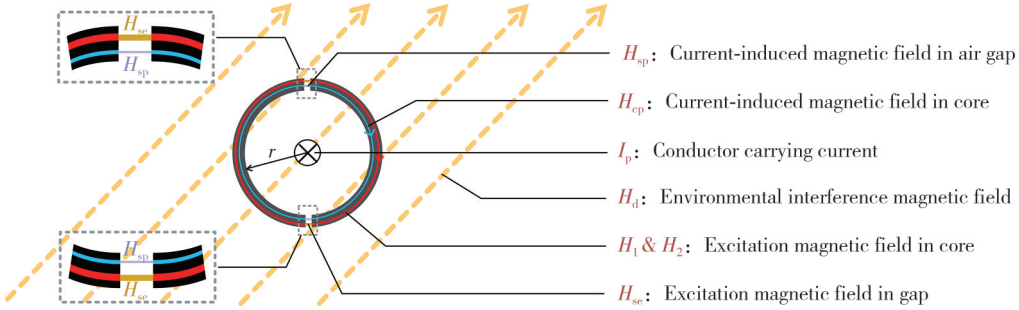

Fig. 2 Magnetic field distribution on core

The total magnetic field is given by $H_{all}=H_{cp}+H_1+H_2+H_d$, i.e.

$$H_{all}=\frac{I_p-4H_{sp}l_s-8H_{se}l_s}{4\pi r-4l_s}+H_d, \tag{6}$$

where the H_d denotes the ambient interference magnetic field.

The magnetic permeability of the core material is a time-varying function $\mu(t)$, the total magnetic induction in the core $B_{all}(t)$, can be expressed based on $B(t)=H\mu(t)$, that is

$$B_{all}(t)=\left(\frac{I_p-4H_{sp}l_s-8H_{se}l_s}{4\pi r-4l_s}+H_d\right)\mu(t). \tag{7}$$

According to Faraday's law of electromagnetic induction, the IEMF can be expressed as

$$E(t)=-2\frac{\partial B}{\partial t}hbw_2, \tag{8}$$

where h is the core width, b the core thickness, and w_2 the number of turns in the induction coil.

Substituting the total magnetic flux density $B_{all}(t)$ into Eq.(8) yields

$$E(t)=-2\frac{\partial B_{all}}{\partial t}hbw_2=$$
$$-2\frac{\partial \mu}{\partial t}\frac{hbw_2(I_p-4H_{sp}l_s-8H_{se}l_s+\pi rH_d-4H_dl_s)}{4\pi r-4l_s}. \tag{9}$$

Performing a Fourier expansion of the magnetic permeability $\mu(t)$ yields

$$\mu(t)=\mu_{0m}+\mu_{2m}\cos(4\pi f_{ex}t)+\mu_{4m}\cos(8\pi f_{ex}t)+\cdots, \tag{10}$$

where μ_{0m} is the static component of the time-varying permeability $\mu(t)$, μ_{2m} and μ_{4m} are the amplitudes of the second and fourth even harmonics, respectively.

Substituting them into Eq.(9), the final IEMF $E_{in}(t)$ can be obtained by

$$E_{in}(t)=-kz,$$
$$k=\frac{2hbw_2(I_p-4H_{sp}l_s-8H_{se}l_s+\pi rH_d-4H_dl_s)}{4\pi r-4l_s},$$
$$z=-4\pi f_{ex}\left(\mu_{2m}\sin(4\pi f_{ex}t)+2\mu_{4m}\sin(8\pi f_{ex}t)+\cdots\right). \tag{11}$$

According to Eq.(11), the IEMF theoretically consists solely of even harmonic components when a current I_p flows through a conductor and is related to the air gap width l_s of the core. Consequently, for the current sensor with a split-core structure, the output performance is inevitably influenced by the air gap. Fortunately, if the air gap is small enough, this effect is not particularly noticeable.

2 Simulation and analysis of fluxgate current sensor

The magnetic core and coil of the measurement probe are simulated, optimized, and analyzed to determine the appropriate parameters. Since the various parameters will affect each other, a quantitative analysis method is selected, that is, analyzing the remaining parameters by giving one of the parameters.

2.1 Selection of core material

The magnetic core of FGCSs needs to reach an alternating saturation state under the excitation signal, which depends critically on the magnetization properties of the core material itself.

Four magnetic material models representing different classes of soft magnetic materials were selected for comparison, as shown in Table 1.

Table 1 Comparison of parameters of four soft magnetic materials

Material type	Saturation flux density B_s/Tesla	Specific conductance $\gamma/(\times10^6\,\mathrm{S\cdot m^{-1}})$	Coercivity $H_c/(\mathrm{A\cdot m^{-1}})$	Relative permeability μ_r
Permalloy 1J85	≈0.66	≈1.79	≈0.80	>12 000
Iron-based amorphous alloy 1K107	≈1.48	≈0.72	≈0.91	>5 000
Iron-nickel-based alloy 2605SC	≈0.92	≈1.43	≈0.84	>10 000
Cobalt-based amorphous alloy VAC6025Z	≈0.53	≈1.58	≈0.65	>20 000

The ideal core material should have low coercivity, low saturation magnetic induction, and high magnetic permeability. After comparing four commonly used magnetic materials, it can be concluded that Vitrovac 6025Z exhibits the best overall performance, followed by Permalloy 1J85 in second place. However, the 6025Z also has some drawbacks: it is harder to obtain and more expensive. In contrast, 1J85 is readily available, and annealed 1J85 exhibits excellent performance. After considering all factors, Permalloy 1J85 has been selected as the core material for the sensor, Fig.3 is its B-H curve.

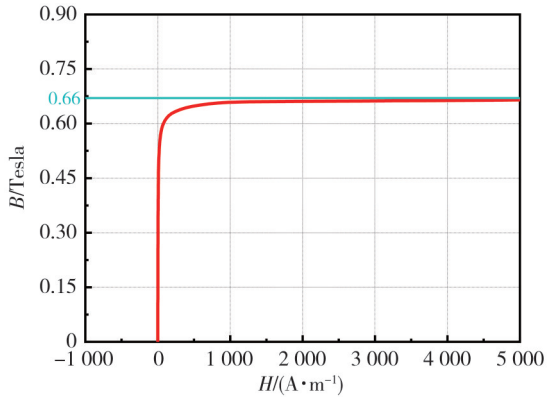

Fig. 3 B-H curve of permalloy 1J85

2.2 Determination of magnetic core size

The radius of the core ring will influence the induction of the external magnetic field. As the core ring radius increases, the magnetic induction on the core weakens, making it necessary to select an appropriately sized radius. A model of an infinitely long straight wire is created, and a magnetic field around it is generated by supplying current to the wire. As shown in Fig.4, a variable distance r is defined between the core and the center of the current-carrying wire. In fact, this distance is the radius of the core ring. Taking the direct current (DC) passing into 2 A as an example, by changing the value of r, we find that the magnetic induction intensity detected on the magnetic core from the magnetic field generated by the current-carrying wire will become weaker and weaker as r increases.

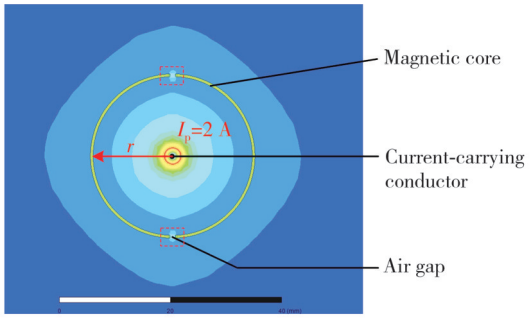

(a) Schematic diagram of core radius optimization

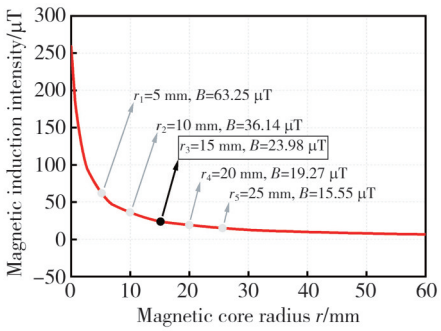

(b) Variation curve of magnetic induction intensity with respect to radius of magnetic core

Fig. 4 Simulation of magnetic induction intensity

This indicates that the radius of the core ring should not be too large in order to obtain higher measurement accuracy in a small range.

Considering that the target range of the designed current sensor is within the 10 A DC range, it was decided to set the radius of the core ring to 15 mm.

If the size of the magnetic core is reduced, more magnetic field can be received, but the number of winding turns of the coil is also limited. Vice versa, a larger core size is more suitable for detecting large current.

After determining the radius of the core ring to be 15 mm, the thickness and width of the core are optimized. To achieve alternating saturation of the core, the excitation signal must be an alternating current (AC) signal. Based on this, the magnetic field generated by the AC signal passing through the excitation coil can be approximated as a plane electromagnetic wave. According to the research[20], the saturation degree of the magnetic core is related to the depth d_k of electromagnetic wave penetration into the interior of the magnetic core, see Fig.5.

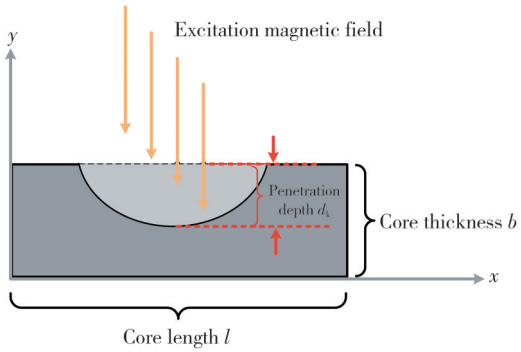

Fig. 5 Effect of excitation magnetic field on core

Fig.5 shows that the thickness of the magnetic core is negatively correlated with its saturation degree at the same frequency. Finally, the expression of EF is derived by

$$f_{ex}=\frac{4}{\pi b^2\gamma\mu}, \tag{12}$$

where b is the core thickness, γ the electrical conductivity, and μ the permeability of the magnetic core.

Following Eq. (12), when the magnetic core material is fixed, the EF is solely dependent on the thickness of the magnetic core, and different thicknesses correspond to different frequencies. In the following simulation optimization, in order to conduct quantitative analysis, we first give the thickness value of the magnetic core, calculate the excitation frequency, and simulate and optimize the remaining parameters at this frequency. Herein, permalloy 1J85 with a thickness of 0.1 mm was selected to fabricate the core. After querying the detailed data for this material, its electrical conductivity is found to be 1.786×10^{6} S/m, and its magnetic permeability is 1.423×10^{-2} H/m. By substituting these parameters into Eq. (12), the matched EF corresponding to the thickness is calculated to be approximately 5 kHz.

Afterward, the width of the magnetic core was optimized. Four sets of core models, all of 0.1 mm thickness and different widths, were set up and placed around them with coil winding. After adding excitation signal to the coils, the number of coil turns was changed to observe the changes in the saturation area ratio (the ratio of the saturation area to the core surface area), according to the B_s=0.66 T of the magnetic core material, we define the area where the magnetic induction intensity exceeds this value as the saturation area, the four sets of core models and their simulation results are shown in Fig. 6. From the test results, it was observed that a wider core is less likely to saturate, whereas a narrower core tends to saturate more easily, even with fewer coil turns. At the same time, it is important to note that while a narrower core may appear advantageous, narrow core sheets are more susceptible to bending and wrinkling during the manufacturing process, which can be detrimental.

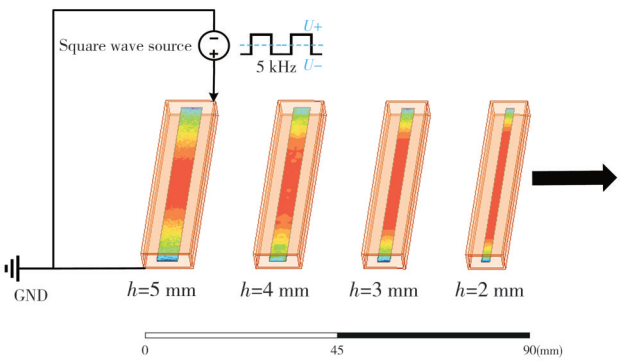

(a) Simulation diagram

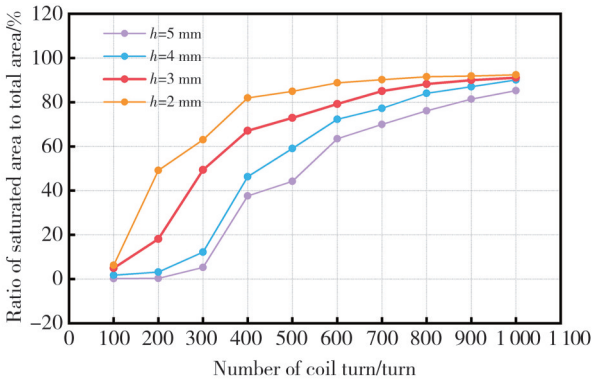

(b) Variation of core saturation area ratio with number of coil turns

Fig. 6 Core saturation changes tests

To this end, we used shearing tools to produce four widths of magnetic core pieces. During the production process, we found that when the width of the magnetic core piece is less than 3 mm, it is easy to bend and deform during the shearing process. Therefore, a core width of 3 mm was chosen as an optimal compromise.

2.3 Optimization of exciting coil

The role of the excitation coil is to generate an AC magnetic field that promotes core saturation. To produce this alternating magnetic field, an AC signal must be applied to the excitation coil. Currently, square, triangle, and sine waves are available as options.

In ideal conditions, the optimal excitation waveform should be a sine wave because it contains almost no remaining harmonic components, this causes it through the excitation coil, there will be less noise coupled to the induction coil. In contrast, the triangular wave signal is less suitable as an excitation signal because its spectral components are rather complex, which will result in a large amount of interference components in the output signal on the sensing side. In the excitation simulation of this paper, we choose square wave excitation for the following reasons.

1) The spectrum of the square wave signal contains higher harmonic components, which is helpful to improve the signal-to-noise ratio (SNR) when using the second harmonic method to demodulate the induction signal.

2) Compared with the sine wave, the high and low level jump of the square wave signal can generate stronger magnetic field changes, thereby enhancing the response to external signals.

3) The square wave signal can be directly generated by the timer of the MCU or FPGA, while the generation of the standard sine wave signal is relatively complex, and the square wave excitation can simplify the excitation circuit.

In the simulation, we use the simplest first-order RL

excitation, and its equivalent circuit diagram is shown in Fig. 7. R_{excoil}, C_{excoil}, and L_{excoil} represent the internal resistance, parasitic capacitance, and inductance of the exciting coil, respectively. R_{limit} is the current-limiting resistor, which helps to ensure that the excitation coil operates in a purely resistive state. However, this condition holds true only if $R_{limit} > Z_{excoil}$, where Z_{excoil} is the impedance of the exciting coil.

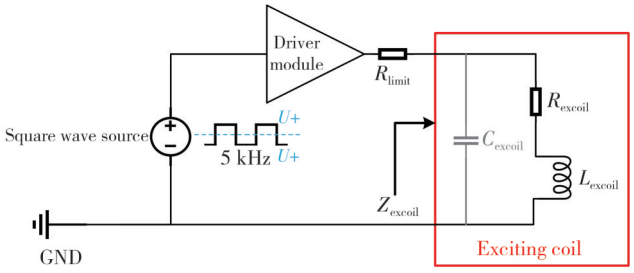

Fig. 7 RL excitation circuit

In the above equivalent circuit, there are

$$Z_{excoil}(s)=(R_{excoil}+sL_{excoil})//\frac{1}{sC_{excoil}}=\frac{R_{excoil}+sL_{excoil}}{s^2L_{excoil}C_{excoil}+sR_{excoil}C_{excoil}+1}. \tag{13}$$

Since the parasitic capacitance C_{excoil} inside the coil is very small, Eq. (13) is simplified as

$$Z_{excoil}(s)=R_{excoil}+sL_{excoil}. \tag{14}$$

Due to the differences in internal resistance and inductance caused by different wire diameters, the excitation coils here uniformly use enameled copper wire with a wire diameter of 0.1 mm. This wire diameter is selected based on its ability to withstand a DC greater than 30 mA. While meeting the needs, it also ensures a sufficient number of turns within a limited volume.

Subsequently, the starting process of the excitation current (EC) is analyzed. As shown in Fig. 8, in one cycle, the core should ideally complete a round of saturation, that is, from t^- to t^+, and back to t^-. It can be seen that the waveform of the EC is a waveform similar to the charging and discharging of a capacitor, Whenever the excitation square wave signal is at a high or low level transition, the EC waveform reaches its peak value. In addition, the excitation current has 9 transition processes in one cycle, namely t^- to t_1, t_1 to t_0, t_0 to t_2, t_2 to t^+, and vice versa. It can be seen that the current changes faster between I_{max} and I_{sat}. This is because when the core begins to saturate, the inductance of the excitation coil decreases, causing its impedance to decrease. Moreover, the decrease in impedance after the core is saturated is much greater than the decrease during the saturation process.

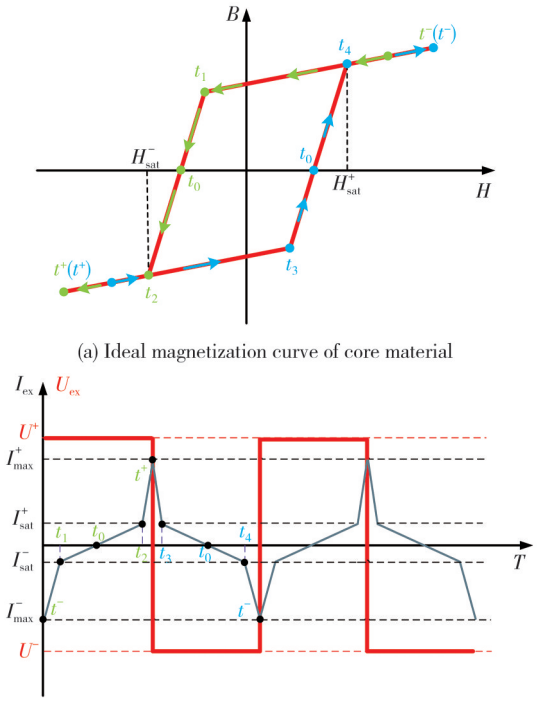

(a) Ideal magnetization curve of core material

(b) Schematic diagram of excitation current oscillation waveform

Fig. 8 Analysis of oscillation process of EC

Building upon this, we conducted a simulation analysis by varying the number of turns of the coil. Fig. 9 illustrates the relationship between the average EC and the number of turns, along with the EC waveforms corresponding to four different turn numbers.

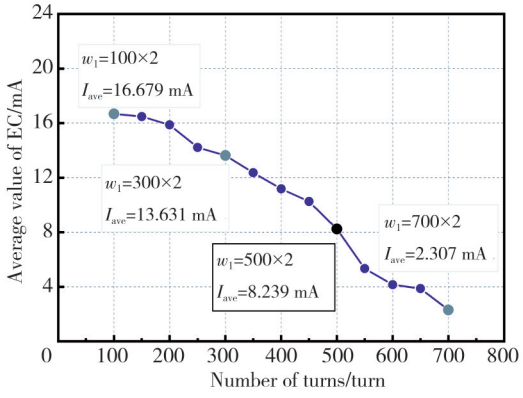

(a) Changes of EC average value with number of turns

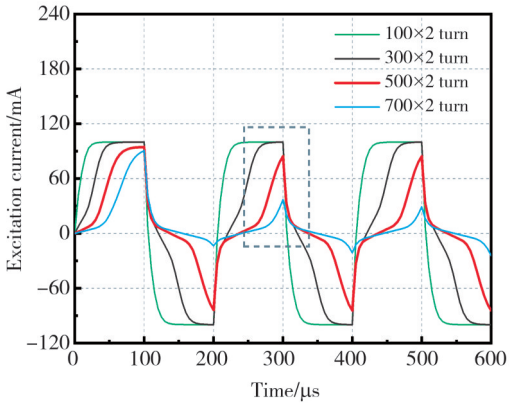

(b) Four groups of EC waveforms with different turns

Fig. 9 Simulation of number of turns in excitation coil

Based on the simulation results, it is observed that as the number of turns of the excitation coil increases, the oscillation amplitude of the EC decreases, which is attributed to the change in its impedance. The ideal EC waveform should exhibit a rapid transition from the negative peak to zero within half a cycle, followed by a shift to the positive peak, and then repeat. If the coil has a small number of turns, the shape of the EC curve is close to the excitation signal, causing the current to be at the peak for too long, resulting in increased power consumption and even heating of the coil; if the coil has a large number of turns, the EC oscillation will be very small and the magnetic core will be difficult to be excited.

To provide sufficient excitation while keeping the waveform as close as possible to the ideal EC curve, we ultimately selected 500 turns for the single-side excitation coil, with a total of 1 000 turns, as the optimal parameters for the sensor. A square wave with an amplitude of 5 V is used for excitation to maintain consistency with the power rail of the subsequent excitation circuit. The corresponding EC waveform and square wave signal under these parameters are shown in Fig.10. It is observed that the EC transitions to the next phase during the level conversion of the square wave signal, completing the transition process within the high or low time period.

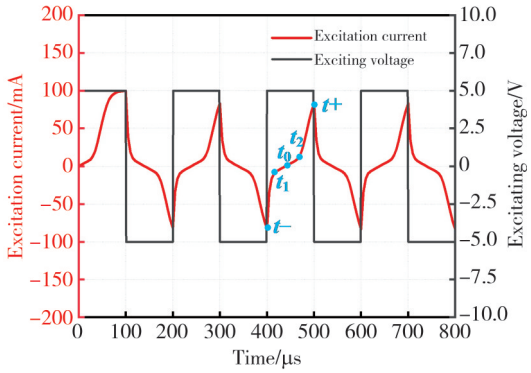

Fig. 10 Diagram of EC waveform with 1 000 turns

In order to more clearly observe the saturation state of the core under the excitation condition, a DC of 2 A was tested and the third cycle of EC for analysis was selected. During this cycle, the EC exhibits a smooth variation. The magnetic flux distribution of the core, obtained from t^- to t^+, is illustrated in Fig.11.

According to Table 1, the saturation magnetic induction intensity B_s of permalloy 1J85 is approximately 0.66 T. As shown in Fig.11, the magnetic induction intensity of the core within the excitation coil reaches above 0.66 T at the point of saturation. More importantly, the core undergoes alternating saturation under the influence of the AC signal. This confirms that the selected number of turns for the excitation coil is appropriately matched.

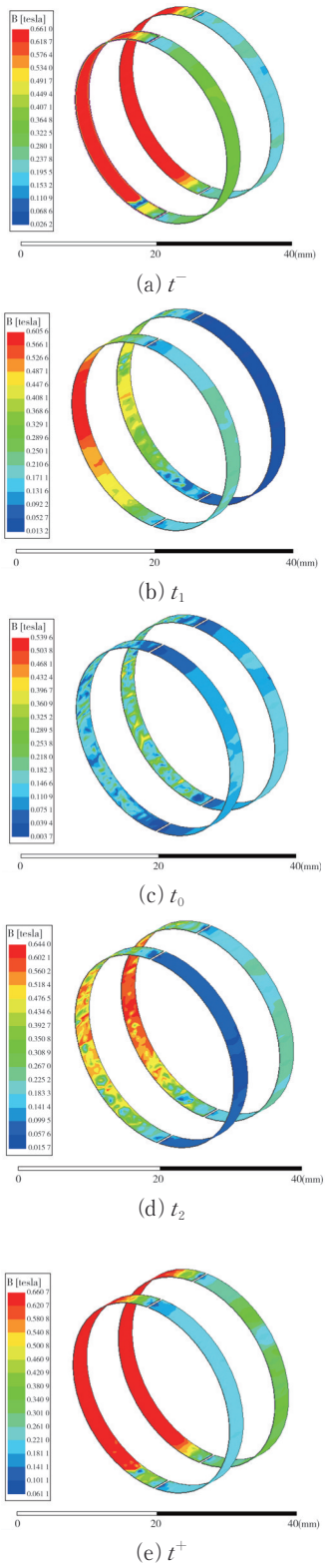

(a) t^-

(b) t_1

(c) t_0

(d) t_2

(e) t^+

Fig. 11 Core saturation from t^- to t^+

2.4 Optimization of induction coil

For the designed split-core sensor structure, two winding methods for the induction coil are proposed. In plan A, the induction coil is wound directly onto the excitation coil. In plan B, the induction coil is wound onto a separate set of cores positioned opposite the

excitation coil. The two winding methods are illustrated in Fig.12.

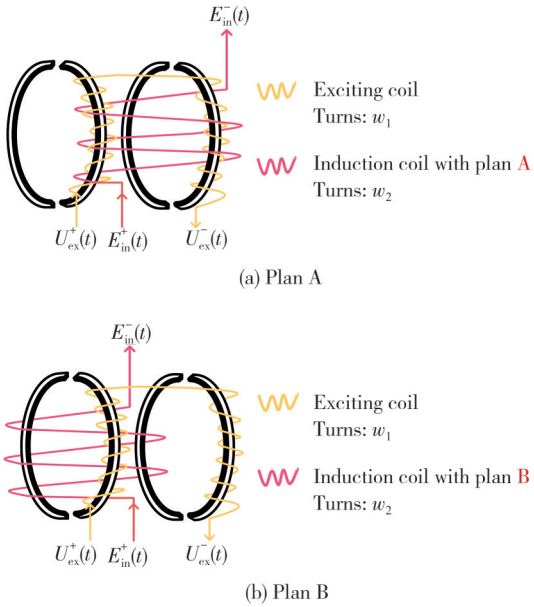

Fig. 12 Induction coil winding mode

The process begins by determining the number of turns for the induction coil. Unlike the exciting coil, the induction coil's primary function is to detect external magnetic fields and generate an IEMF. While increasing the number of turns can enhance the magnitude of the second harmonic of the IEMF, it also increases the coil's equivalent inductance and capacitance. As a result, the harmonic signal of other orders is also enhanced, which reduces the SNR.

We still take the 2 A measured current as an example, when a DC current flows through the conductor, the spectrum of the IEMF is analyzed by varying the number of coil turns. The first, second, third and fourth harmonic components, which contribute significantly to the signal, are then isolated and subjected to data fitting. Fig.13 shows the variation of the amplitude of each harmonic component of the output IEMF signal with the number of turns under different induction coil winding modes.

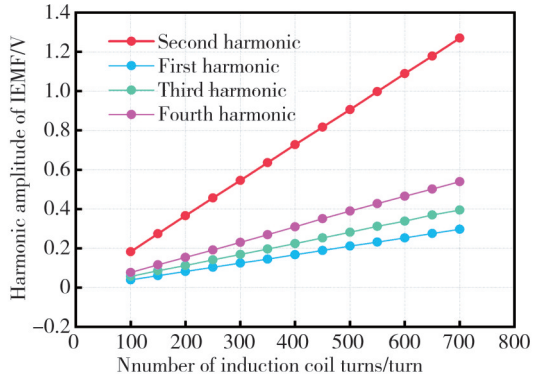

(a) Changes of several harmonics with induction coil under plan A

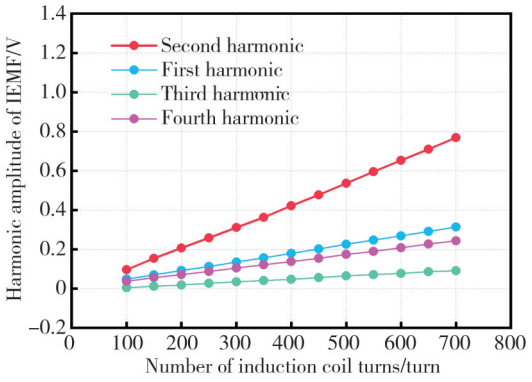

(b) Changes of several harmonics with induction coil under plan B

Fig. 13 Simulation of two winding methods

It can be concluded that due to the magnetic leakage effect, the overall performance of plan B is inferior to that of plan A. Furthermore, as the number of turns increases, the second harmonic grows, accompanied by an increase in several other irrelevant components. It is important to note that this analysis is based on an ideal simulation. In actual production, the situation may be even more detrimental.

Like the excitation coil, the equivalent impedance Z_{incoil} of the induction coil can also be expressed as

$$Z_{incoil}(s) = R_{incoil} + sL_{incoil}, \tag{15}$$

where R_{incoil} and L_{incoil} represent the internal resistance and inductance of the induction coil, respectively.

As the number of turns increases, the second harmonic amplitude also rises. However, this leads to higher impedance, which in turn amplifies noise interference, necessitating a trade-off. To optimize the SNR while maintaining a higher number of turns, we use 0.2 mm diameter enameled copper wire (which is thicker than the wire used in the excitation coil) to wind the induction coil with 300 turns. In conclusion, we derived the time-domain and frequency-domain waveforms of the induced electromotive force for the 300-turn coil under both schemes, which further validated the aforementioned analysis.

Consistent with the analysis, as shown in Fig.14, the dual-core structure of the sensor enables the generation of IEMF twice per cycle, and plan A produces a higher amplitude of IEMF.

The waveform is smoother, more regular, and exhibits less noise. Moreover, the second harmonic amplitude generated by plan A is significantly greater, reaching 0.545 V. As a result, a stronger induced signal occurs when the induction coil is positioned closer to the excitation coil in the presence of an external magnetic field. Winding the induction coil on the excitation coil proves to be more effective.

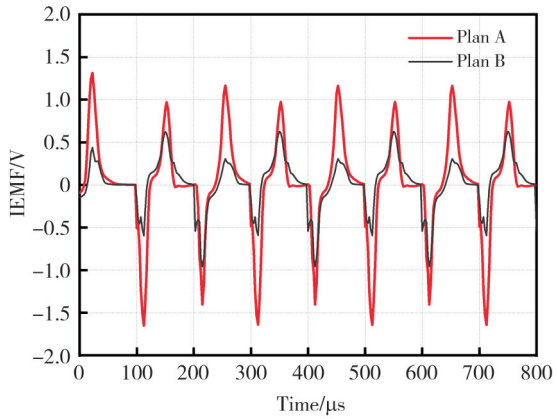

(a) Comparison of two IEMF methods

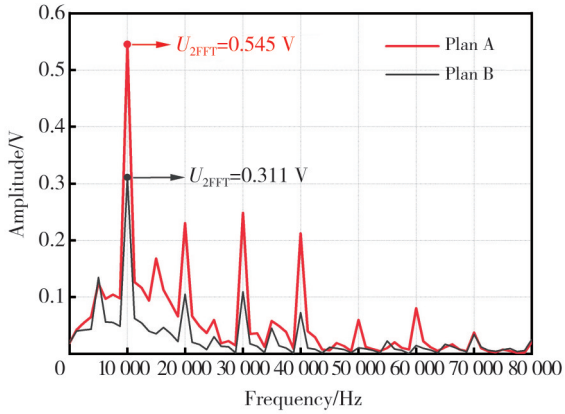

(b) Comparison of two IEMF FFT methods

Fig. 14 Simulation of two winding methods

As a final step, a feedback coil is incorporated to generate a compensating current, bringing the sensor closer to a zero-flux condition. Since this design is for ±10 A DC measurement, the number of turns of the feedback coil can be appropriate. Here, 600 turns of 0.2 mm diameter enameled copper wire are used. According to Ampère's loop law, the magnetic field generated by the current-carrying wire B_p can be expressed by

$$B_p = \frac{\mu_0 I_p}{2\pi r}, \tag{16}$$

where μ_0 is the vacuum permeability, $4\pi \times 10^{-7}$ T·m/A.

Similarly, the magnetic field generated by the feedback coil can be expressed as

$$B_{feedback} = \frac{600\mu_0 I_{feedback}}{2\pi r}, \tag{17}$$

where $I_{feedback}$ is the feedback current.

Under such conditions, only a small feedback current is required to generate a significant feedback magnetic field. Consequently, the optimization of the simulation parameters of the entire current sensor probe is thus completed.

3 Experimental and analysis of current sensors

3.1 Sensor probe fabrication

Based on the simulation results, a current sensor probe prototype was constructed. The resistance of each coil and the inductance of the induction coil were measured, yielding an inductance of approximately 2.88 mH. To facilitate the subsequent tuning of the induction signal, a resonant capacitor C_r is connected in parallel at both ends of the induction coil, thereby forming an LC resonance circuit, tuned to the frequency of the second harmonic at 10 kHz. To achieve this, the value of the tuning capacitor C_r can be calculated by

$$C_r = \frac{1}{(2\pi f_{sh})^2 L_{incoil}}, \tag{18}$$

where f_{sh} is the second harmonic frequency.

Substituting the value of the inductance of the induction coil into Eq. (18) yields a resonant capacitance C_r value of approximately 87.95 nF.

To achieve the objective, the actual resonant capacitor was formed by connecting 82 nF and 6.8 nF in parallel. Table 2 lists the parameters of the sensor probe, and the fabricated sensor probe is shown in Fig. 15. For the fabrication of the sensor probe, the coil skeleton and housing were first modeled using Solidworks. Secondly, the core material is annealed and cut to remove internal stress and reduce hysteresis loss. After the modeling was completed, 3D printing was performed. The coil was then wound onto the corresponding skeleton, and the magnetic core was inserted. Finally, the components were assembled, completing the structural integration of the probe. Additionally, after the circuit module design was finalized, the probe was soldered onto the circuit board.

Table 2 Sensor probe parameters

Parameter	Value
Wire diameter of exciting coil p_1/mm	0.1
Number of excitation coil turns w_1/turn	1 000
Internal resistance of excitation coil R_1/Ω	21.9
Wire diameter of induction coil p_2/mm	0.2
Number of induction coil turns w_2/turn	300
Induction coil internal resistance R_2/Ω	8.1
Wire diameter of feedback coil p_3/mm	0.2
Number of feedback coil turns w_3/turn	600
Feedback coil internal resistance R_3/Ω	12.2
Radius of magnetic core r/mm	15
Magnetic core width h/mm	3
Width of air gap l_s/mm	0.5

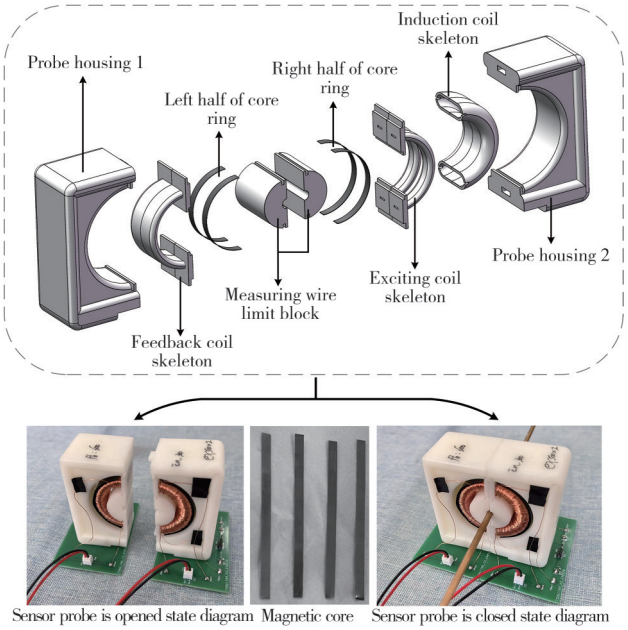

Fig. 15 Sensor probe structure and its real photos

3.2 RLC excitation circuit design

The previous simulation analysis used ±5 V square wave signals as the excitation conditions. However, in the actual circuit, the full-bridge square wave may introduce higher-order harmonic noise interference, necessitating the use of a dual-power supply for the corresponding drive module. To mitigate noise, a blocking capacitor C_b is added in series to the excitation circuit, and the signal amplitude is adjusted to +5 V. This setup converts the excitation into an RLC series configuration as shown in Fig.16.

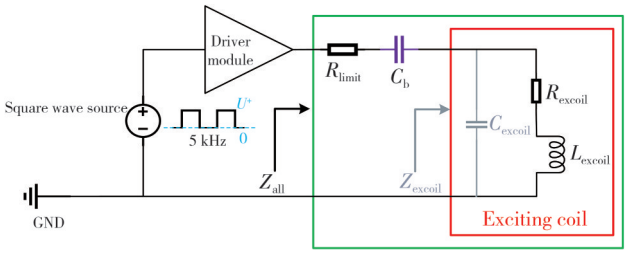

Fig. 16 RLC excitation circuit

In this configuration, we only need to use an AMS1117-5.0 +5 V voltage regulator chip and a TC4422 driver chip to complete the construction of the excitation circuit's drive section. For the capacitor C_b, it is preferable to select a value that ensures the charging and discharging processes are completed within one cycle of the square wave.

According to Fig. 16, the total impedance Z_{all} of the excitation part is

$$Z_{all}(s)=R_{limit}+\frac{1}{sC_b}+Z_{excoil}(s)=$$

$$R_{limit}+R_{excoil}+sL_{excoil}+\frac{1}{sC_b}=$$

$$\frac{s^2+\dfrac{(R_{limit}+R_{excoil})}{L_{excoil}}s+\dfrac{1}{L_{excoil}C_b}}{\dfrac{s}{L_{excoil}}}, \tag{19}$$

where R_{limit} is current-limiting resistor. Therefore, the damping factor is expressed as

$$\xi=\frac{R_{limit}+R_{excoil}}{2}\sqrt{\frac{C_b}{L_{excoil}}}. \tag{20}$$

Therefore, the selection of C_b should try to achieve the critical damping state of the circuit. Improper selection of C_b can lead to over-damping or under-damping in the circuit, preventing the EC from fully discharging when the square wave transitions between high and low levels.

Several capacitors are selected for multiple tests (see Fig.17).

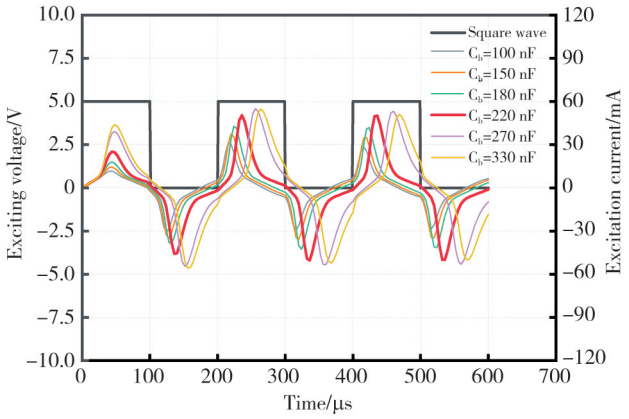

(a) EC corresponding to different C_b

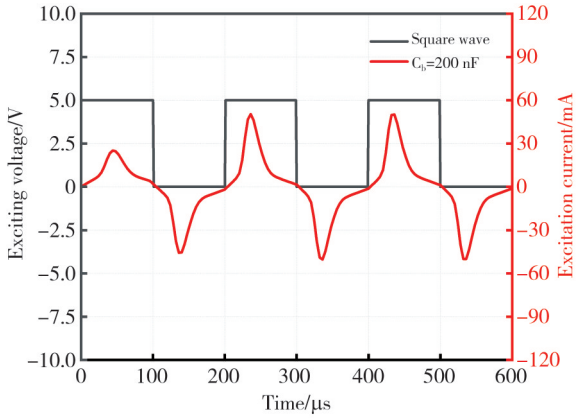

(b) EC when C_b=220 nF

Fig. 17 Simulation of C_b

For the excitation coil with an internal resistance of approximately 21.9 Ω, the C_b value of 220 nF was chosen to ensure that the charging and discharging process of the EC, from 0 mA to its peak value and back to 0 mA, occurs within the high or low phase of the excitation signal. In addition, the function of the current limiting resistor is to prevent excessive current from entering the excitation coil and causing heating. Its selection should be slightly larger

than the internal resistance of the coil. Here, R_{limit} is selected as 30 Ω because if R_{limit} is too large, the EC peak value will be reduced, thereby reducing the excitation magnetic field, which is not conducive to the saturation of the magnetic core. When the excitation coil is working, its EC peak I_{m} value is

$$I_{\text{m}} = \frac{U_{\text{ex}}}{\sqrt{\left(R_{\text{limit}} + R_{\text{excoil}}\right)^2 + \left(2\pi f_{\text{ex}} L_{\text{excoil}} - \dfrac{1}{2\pi f_{\text{ex}} C_{\text{b}}}\right)^2}} \tag{21}$$

After constructing the RLC excitation circuit, it is confirmed whether the circuit is working properly by observing whether the waveform of the excitation electromotive force (EEMF) at both ends of the excitation coil presents a periodic oscillation.

By comparing the EEMF waveforms at both ends of the excitation coil in the simulation and the actual circuit (as shown in Fig.18), it is evident that the simulated and measured waveforms exhibit a high degree of consistency.

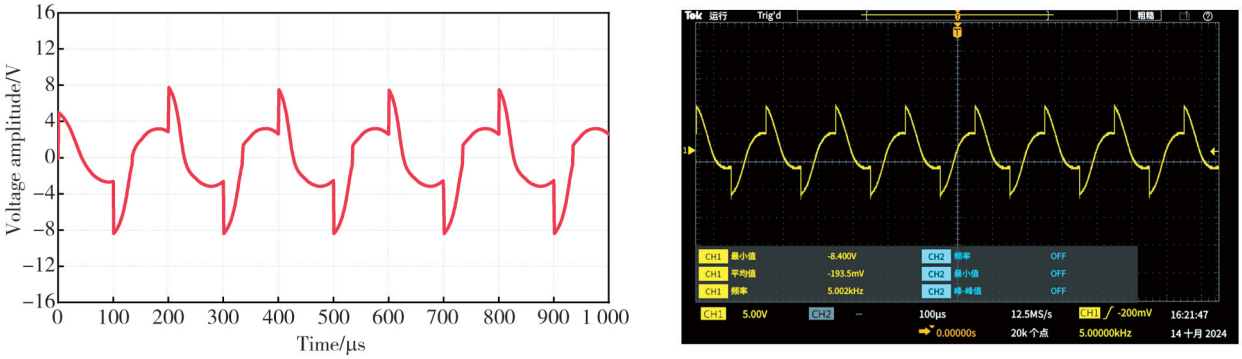

(a) Simulation result

(b) Actual test result

Fig. 18 EEMF output results

When a 5 kHz square wave signal is applied to the coil through the excitation circuit, periodic oscillations occur, and whenever the excitation square wave undergoes a high-low level transition, the EEMF also undergoes an obvious mutation at this moment, indicating that the excitation coil is operating as expected.

3.3 Signal processing circuit design

The design of the signal processing circuit is based on the second harmonic demodulation method. As the induced electromotive force comprises a superposition of multiple odd and even harmonics, with the second harmonic being the most dominant, it must be extracted. This is achieved through LC resonance, followed by amplification, filtering, phase-sensitive detection, and rectification, ultimately producing a DC voltage that represents both the magnitude and direction of the measured DC current.

To demodulate the second harmonic, a signal processing circuit (as shown in Fig.19) was developed.

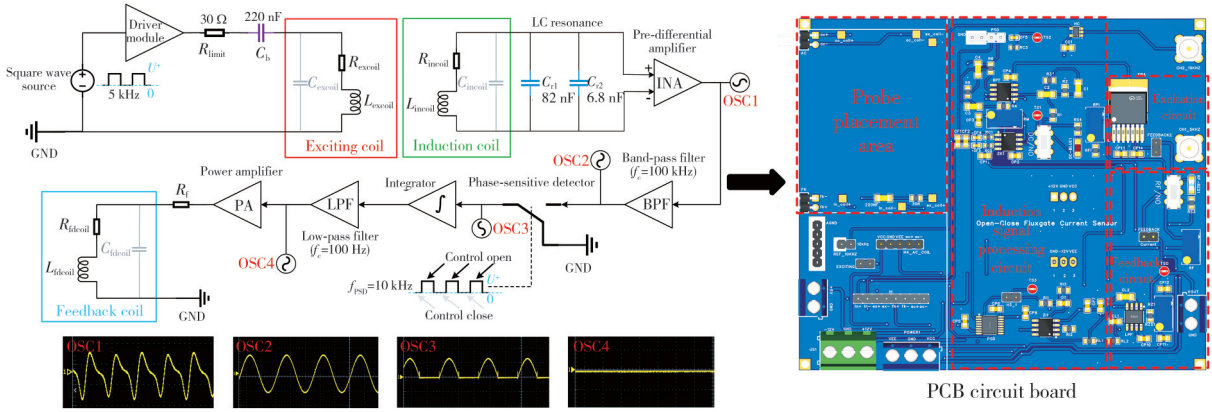

Fig. 19 Sensor excitation and signal processing circuit

The circuit comprises an LC resonant circuit, an instrumentation amplifier (INA), a band-pass filter (BPF), a phase-sensitive detector (PSD), an integrator (INT), a low-pass filter (LPF), and a feedback loop. The feedback loop includes a feedback resistor and a power amplifier (PA). The signal processing circuit is powered by a multi-channel linear power supply (supply voltage ±12 V), while the excitation and reference signals are generated by the FPGA signal generator. Waveforms at the four test points (OSC1 to OSC4) were captured using an

oscilloscope, and the obtained output waveforms matched the expected results.

The entire working process is as follows. Initially, the induced signal is amplified by the INA after passing through the LC resonance, and then filtered by the BPF to obtain the 10 kHz second harmonic signal. The signal passes through the PSD. If the measured current flows in the forward direction, the phase of the second harmonic sinusoidal signal aligns with the input square wave signal. If the current is in the reverse direction, the phase is inverted. The 10 kHz sinusoidal signal is then split into half-waves, which are processed through the integrator and LPF, resulting in a DC signal that reflects both the magnitude and direction of the measured current. This DC signal then enters the feedback coil, generating a feedback magnetic field and achieving a near-zero magnetic flux condition.

3.4 Experimental test system construction

The overall experimental test system built is illustrated in Fig.20.

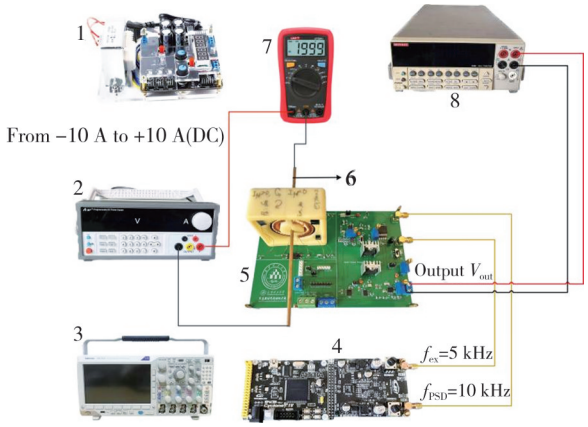

Fig. 20 Fluxgate current sensor experimental test system

The experimental setup is as follows. 1) Multi-rail linear power supply. 2) High-precision DC power supply. 3) Oscilloscope. 4) FPGA signal generators. 5) The designed split-core FGCS prototype. 6) Copper rods. 7) Digital multimeter. 8) High precision voltmeter.

In this setup, an oscilloscope was used for functional debugging of each circuit module, while a high-precision DC power supply was used to deliver currents of varying magnitudes and directions to the copper bar, thereby simulating the current-carrying conductor under test. Finally, a digital multimeter was connected to the designated output terminal of the circuit to monitor the sensor's output voltage in real-time.

For experimental equipment, the oscilloscope used was the Tektronix TBS-1102C model, featuring a 100 MHz bandwidth and a maximum sampling rate of 1 GS/s. The DC power supply was the A-BF SS-L303SPD high-precision regulated power supply, with an output current accuracy of 0.01 mA. The multimeter used was the Keithley 2000, offering a resolution of six and a half digits and an voltage measurement accuracy of up to 0.002%. The power supply of the PCB board uses an adjustable multi-rail linear power supply with an output ripple of less than 5 mV, which can ensure the normal operation of the board-level circuit. Finally, a multimeter was used to detect the current size in the current-carrying wire. A four-and-a-half-digit Uni-T multimeter, model UT33B+, is used, which can meet the current measurement within 10 A.

3.5 Performance testing and analysis

After the sensor prototype was fabricated and the experimental testing system was established, its output sensitivity, linearity, repeatability, and hysteresis error were tested and analyzed. The test was conducted sequentially within the ±10 A range, with a step size of 0.5 A. The important point is that the output voltage value measured by a high-precision multimeter retains four decimal places. The obtained fitting data are shown in Fig.21.

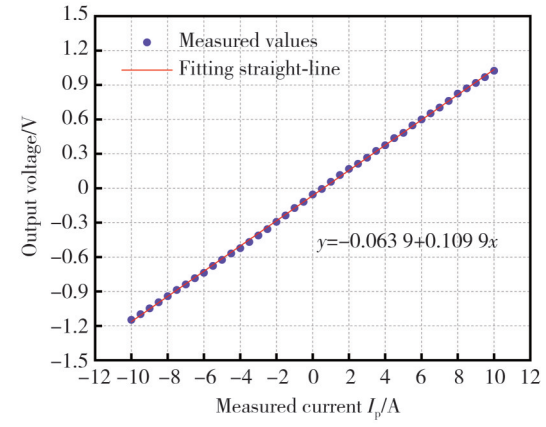

(a) Linearity test

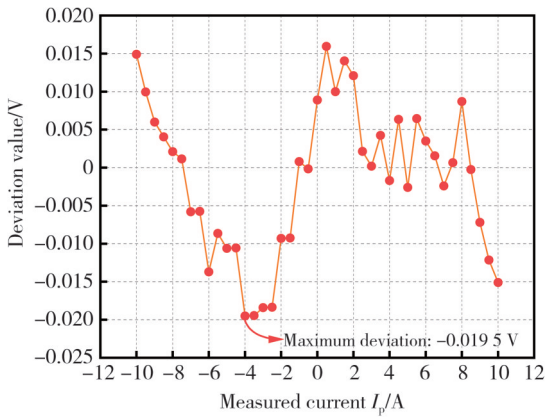

(b) Measuring error test

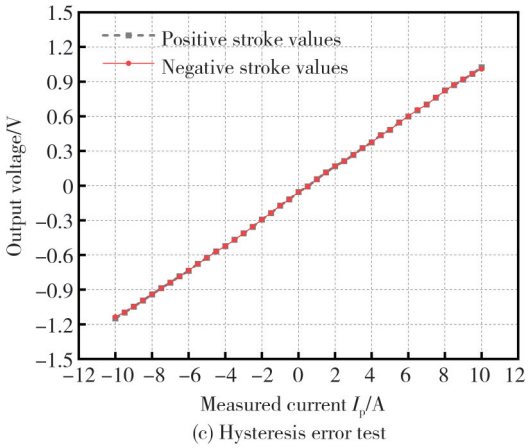

(c) Hysteresis error test

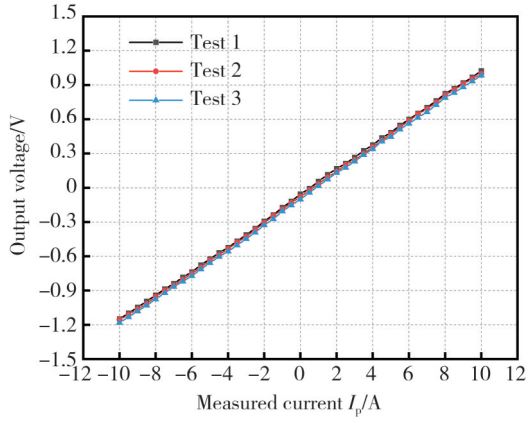

(d) Repeatability test

Fig. 21 Sensor performance test results

First, based on the fitting results of the previous two sets, the linearity is found to be 0.856%, and the sensitivity is 0.109 9 V/A. Subsequently, the hysteresis error is tested, the positive and negative stroke output values of the sensor are obtained by gradually adjusting the measured current from −10 A to +10 A, and then reversing the adjustment back to −10 A. According to the results of the fitting, the maximum deviation of the positive and negative stroke output is found to be 0.019 5 V at −10 A. With the hysteresis factor set to 1, the hysteresis error is calculated to be 0.559%, which is within an acceptable range. Ultimately, repeatability tests are conducted. It can be observed that the output voltage of the sensor exhibits a certain degree of drift in all three tests, which may be attributed to weak external magnetic interference. After fitting and calculation, the repeatability is determined to be 1.574%, which meets the expected value.

As a result of using Permalloy 1J85 as the magnetic core material, which has relatively lower magnetic permeability, saturation magnetic induction, and other magnetic properties compared to cobalt-based amorphous alloys, coupled with the open magnetic circuit design, the sensor's performance is somewhat limited. Nevertheless, the final test results show that the overall performance remains within a tolerable range.

In order to further reduce the nonlinear error, the polynomial fitting method is used[21]. In the code, a cubic polynomial is constructed to fit the relationship between the measured current I_p and the output voltage.

$$V_{output} = aI_p^3 + bI_p^2 + cI_p + d. \tag{22}$$

We determine the coefficients a, b, c, and d by fitting the given dataset using a nonlinear regression function. Then, the fitted polynomial function is used to calculate the compensated output voltage, thereby correcting nonlinear errors. The compensation results are shown in Fig.22.

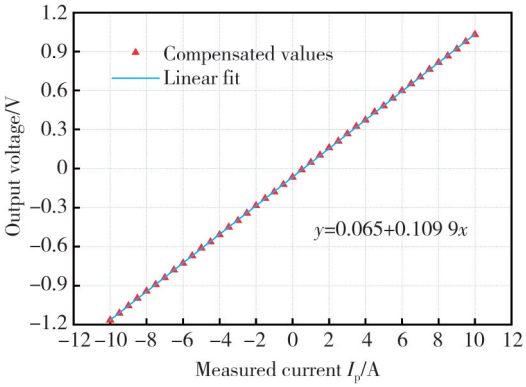

(a) Linearity test

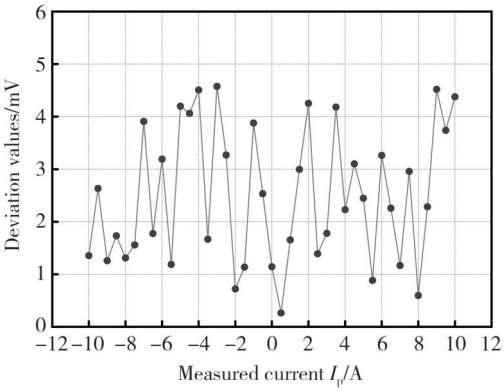

(b) Measuring error test

Fig. 22 Fitting results after compensation

Finally, the nonlinear error is reduced to 0.208%, and the maximum deviation was 4.577 mV. The remaining two current sensors were selected for performance comparison, as shown in Table 3.

Table 3 Comparison of performance parameters

Sensor	Measuring range	Nonlinearity error/%	Structure
Design of this paper	±10 A	0.208	Split-core type
Sensor[18]	±5 A	0.223	Split-core type
Hangzhi RIT10M[22]	±10 A	<0.2	Closed-core type

After comparison, the split-core type FGCS developed in this paper not only has little difference in performance with the closed-core type, but also provides convenience

for isolated measurement.

4 Conclusions

In this paper, a split-core DC current sensor is developed based on the fluxgate principle, and the following is mainly accomplished.

1) On the basis of the traditional closed double-core type fluxgate current sensor, the magnetic core is divided into two symmetrical four parts, so as to realize the purpose of flexible measurement. After that, according to the structural characteristics, the mathematical model of induced electromotive force under the working condition is deduced.

2) Using the finite element analysis method to optimize the simulation parameters of the core radius, core width, number of turns of the excitation coil, induction coil winding method and number of turns of the induction coil, the sensor probe is made according to the optimized results, and the corresponding excitation circuit and signal processing circuit are built.

3) The performance test of the sensor prototype is carried out by building an experimental test platform, and the nonlinear error is compensated. The final test results show that the sensor has a sensitivity of 0.109 9 V/A, a nonlinear error of 0.208%, a hysteresis error of 0.559%, and a repeatability error of 1.574% over a measurement range of ±10A. After comparison, the performance is close to that of a commercial sensor with a closed magnetic circuit.

In future research work, the optimization of the circuit module can be continued to make the sensor more intelligent, while the design of a matching magnetic shielding case for the sensor is expected to further improve its performance.

Acknowledgement

This work was supported by Yunnan Fundamental Research Projects (No. 202301AT070181), Yunnan Fundamental Research Projects (No.202401CF070126), Xingdian Talent Support Program of Yunnan Province (No. KKRD202203070); Yunnan High level Science and Technology Talents and Innovation Team Selection Special Project (No.202405AS350001).

Declaration of conflicting interests

The authors have no conflict of interests related to this publication.

References

[1] ZHANG S Q, ZHANG J F, LIU F, et al. Development of a cryogenic DC transformer using for the measurement of large current. Journal of Instrumentation, 2024, 19(2): P02023.

[2] TAN X Y, LI W Y, QIAN G C, et al. Design of a fluxgate weak current sensor with anti-low frequency interference ability. Energies, 2022, 15(22): 8489.

[3] WANG L S, HAN Y L, JI Y F, et al. Large bandwidth and dynamic range current sensor based on micro-PCB Rogowski coil. Measurement Science and Technology, 2024, 35(5): 055107.

[4] GIBIINO G P, MARCHESI M, COGLIATI M, et al. Experimental evaluation of Hall-effect current sensors in BCD10 technology. Measurement, 2023, 220: 113289.

[5] CRESCENTINI M, SYEDA S F, GIBIINO G P. Hall-effect current sensors: principles of operation and implementation techniques. IEEE Sensors Journal, 2022, 22(11): 10137-10151.

[6] LIN W C, WU C Y, LIAO C H, et al. Study and implementation of fluxgate current sensor with wireless connectivity for finger exoskeleton rehabilitation. International Journal of Circuit Theory and Applications, 2024, 52(1): 1-15.

[7] MOHNS E, ROEISSLE G, FRICKE S, et al. An AC current transformer standard measuring system for power frequencies. IEEE Transactions on Instrumentation and Measurement, 2017, 66(6): 1433-1440.

[8] SHARIFINIA S, ALLAHBAKHSHI M, GHANBARI T, et al. A new application of Rogowski coil sensor for partial discharge localization in power transformers. IEEE Sensors Journal, 2021, 21(9): 10743-10751.

[9] BRYAKIN I V, BOCHKAREV I V, KHRAMSHIN V R, et al. Fluxgate sensor with bifactor excitation mode. Sensors, 2023, 23(4): 1775.

[10] SCHRITTWIESER L, MAUERER M, BORTIS D, et al. Novel principle for flux sensing in the application of a DC+AC current sensor. IEEE Transactions on Industry Applications, 2015, 51(5): 4100-4110.

[11] XIAO X, SONG H T, LI H B. A high accuracy AC+DC current transducer for calibration. Sensors, 2022, 22(6): 2214.

[12] LI J J, REN W, LUO Y S, et al. Design of fluxgate current sensor based on magnetization residence times and neural networks. Sensors, 2024, 24(12): 3752.

[13] WANG N, ZHANG Z H, LI Z K, et al. Design and characterization of a low-cost self-oscillating fluxgate transducer for precision measurement of high-current. IEEE Sensors Journal, 2016, 16(9): 2971-2981.

[14] WEI Y T, WANG Y, WANG M L, et al. Digital fluxgate current sensor based on second harmonic detection. International Journal of Applied Electromagnetics and Mechanics, 2020, 64(1/2/3/4): 111-118.

[15] YANG W C, XIE X G, YANG Q, et al. Design and

hardware experiment of concentrating magnetic ring of current sensors used in open-loop fluxgate. Frontiers in Energy Research, 2022, 10: 926343.
[16] YANG X G, LI Y Y, GUO W, et al. A new compact fluxgate current sensor for AC and DC application. IEEE Transactions on Magnetics, 2014, 50(11): 4005704.
[17] LEI H Y. Research and design of DC current sensor based on zero-magnetic-flux principle. Chengdu: University of Electronic Science and Technology of China, 2023.
[18] SONG K Q. Design of fluxgate current sensor based on dual-core open magnetic circuit structure. Dissertation for the Master Degree. Hangzhou: Hangzhou Dianzi University, 2022.
[19] FIOLHAIS M C N, ESSÉN H, PROVIDÊNCIA C, et al. Magnetic field and current are zero inside ideal conductors. Progress In Electromagnetics Research B, 2011, 27: 187-212.
[20] BARRIOS E L, URTASUN A, URSÚA A, et al. Optimal DC gapped inductor design including high-frequency effects//IECON 2015-41st Annual Conference of the IEEE Industrial Electronics Society, November 9-12, 2015, Yokohama, Japan. New York: IEEE, 2016: 3928-3933.
[21] WANG N. Self-oscillating fluxgate technology for precision measurement of DC high current. Harbin: Harbin Institute of Technology, 2016.
[22] Shenzhen Hangzhi Precision Electronics Co., Ltd. Datasheet for RIT10M Current Sensor version 1.0. 2023.

开合式磁通门直流电流传感器仿真参数优化与研制

杨德超[1], 施俊江[1], 赵振刚[1,2*], 侯瑛杰[1], 杨旭松[1], 蒋 欣[1]

1. 昆明理工大学 信息工程与自动化学院, 云南 昆明 650500;
2. 云南省绿色能源与数字电力量测及控保重点实验室, 云南 昆明 650500

摘 要： 磁通门电流传感器凭借其高精度特性在电力系统中的应用日益广泛，但传统磁通门电流传感器的闭合磁芯设计使其测量灵活性受限。本文提出一种采用四磁芯条构成的开合式传感器结构，在保持测量精度的同时实现非侵入式电流检测。基于所设计的传感器探头结构建立了感应电动势数学模型，通过有限元仿真对磁芯半径、磁芯宽度、激励线圈匝数以及感应线圈构型进行了参数优化与分析，研制了包含测量探头、激励电路和信号处理电路的传感器原型并完成性能测试。实验结果表明：在±10 A的测量范围内具有0.109 9 V/A的灵敏度、0.559%的迟滞误差和1.574%的重复性误差。经多项式拟合法进行误差补偿后，非线性误差降低至0.208%，与采用闭合磁芯结构的传感器性能相当。该研究为需兼顾高精度与安装灵活性的应用场景提供了实用化解决方案。

关键词： 磁通门电流传感器；二次谐波法；有限元仿真；参数优化；电路设计；直流电测量

引用格式： YANG Dechao, SHI Junjiang, ZHAO Zhengang, et al. Simulation-based parameter optimization and development of a split-core fluxgate DC current sensor. Journal of Measurement Science and Instrumentation, 2025, 16(4): 588-602. DOI: 10.62756/jmsi.1674-8042.2025057